Ocean Dynamics (2013) 63:1189–1201
DOI 10.1007/s10236-013-0656-7

The TKE dissipation rate in the northern South China Sea

Iossif Lozovatsky · Zhiyu Liu · Harindra Joseph S. Fernando · Jianyu Hu · Hao Wei

Received: 5 February 2013 / Accepted: 19 September 2013 / Published online: 19 October 2013

Abstract The microstructure measurements taken during the summer seasons of 2009 and 2010 in the northern South China Sea (between 18°N and 22.5°N, and from the Luzon Strait to the eastern shelf of China) were used to estimate the averaged dissipation rate in the upper pycnocline $\langle \varepsilon_p \rangle$ of the deep basin and on the shelf. Linear correlation between $\langle \varepsilon_p \rangle$ and the estimates of available potential energy of internal waves, which was found for this data set, indicates an impact of energetic internal waves on spatial structure and temporal variability of $\langle \varepsilon_p \rangle$. On the shelf stations, the bottom boundary layer depth-integrated dissipation $\widehat{\varepsilon}_{BBL}$ reaches 17–19 mW/m^2, dominating the dissipation in the water column below the surface layer. In the pycnocline, the integrated dissipation $\widehat{\varepsilon}_p$ was mostly ~10–30 % of $\widehat{\varepsilon}_{BBL}$. A weak dependence of bin-averaged dissipation $\overline{\varepsilon}$ on the Richardson number was noted, according to $\overline{\varepsilon} = \varepsilon_0 + \frac{\varepsilon_m}{(1+Ri/Ri_{cr})^{1/2}}$, where $\varepsilon_0 + \varepsilon_m$ is the background value of $\overline{\varepsilon}$ for weak stratification and Ri_{cr}=0.25, pointing to the combined effects of shear instability of small-scale motions and the influence of larger-scale low frequency internal waves. The latter broadly agrees with the MacKinnon–Gregg scaling for internal-wave-induced turbulence dissipation.

Keywords Turbulence · Internal waves · South China Sea

Responsible Editor: Pierre De Mey

I. Lozovatsky · H. J. S. Fernando
Environmental Fluid Dynamics Laboratories, Department of Civil & Environmental Engineering and Earth Sciences, University of Notre Dame, Notre Dame, IN 46556, USA

Z. Liu · J. Hu
State Key Laboratory of Marine Environmental Science, and Department of Physical Oceanography, College of Ocean & Earth Sciences, Xiamen University, 422 Siming South Road, Xiamen 361005, China

H. Wei
College of Marine Science and Engineering, Tianjin University of Science & Technology, Tianjin 300457, China

Z. Liu (✉)
Room C3-416 Xiping Building, Xiangan Campus, Xiamen University, Xiamen 361102, China
e-mail: zyliu@xmu.edu.cn

1 Introduction

The northern South China Sea (SCS) has a deep (>2,000 m) central basin and a wide continental shelf of depths less than 200 m. In recent years, the deep northern basin of SCS has been actively investigated for generation, propagation, and breakdown of large-amplitude nonlinear internal waves (NLIW) (e.g., Orr and Mignerey 2003; Duda et al. 2004; Gawarkiewicz et al. 2004; Duda and Rainville 2008; Huang et al. 2008; Ramp et al. 2010; Alford et al. 2010; Farmer et al. 2011). Internal waves (IW) and mixing in this region are strongly affected by barotropic tide and main patterns of SCS circulation, which are coupled to short-term variations of atmospheric forcing. In particular, such powerful events as tropical cyclones (typhoons) in the western Pacific and China Seas, frontal dynamics, and the bottom topography that controls water exchange between shallower and deeper basins play key roles.

The tidal currents in SCS rotate clockwise, being driven by the diurnal O_1 and K_1 constituents over the upper slope and the semidiurnal constituent M_2 over the shelf (Beardsley et al. 2004). The semidiurnal S_2 constituent is also enhanced on the shelf, but it is always weaker than O_1 and K_1. Mesoscale eddies of various sizes have been observed in the northern SCS, near Dongsha Islands, and to the west of the Luzon Strait.

High-amplitude NLIW generated in the Luzon Strait region propagate northwestwards (Huang et al. 2008; Simmons et al. 2011). Basic characteristics of NLIW have been obtained using SAR images (e.g., Liang et al. 1995; Hsu et al. 2000; Liu and Hsu 2004; Huang et al. 2008) and mooring measurements (e.g., Duda et al. 2004; Yang et al. 2004; Lien et al. 2005; Chang et al. 2006; Duda and Rainville 2008; Alford

et al. 2010; Ramp et al. 2010; Li and Farmer 2011). The NLIW are mostly observed between 19°N and 22°N, with crest lengths ~100–250 km, propagating speeds ~0.3–3.0 m/s, and amplitudes ~2–150 m. About 70 % of annual IW signatures on SAR images were observed in the summertime while a seasonal minimum (only 1 %) was registered in the winter (Huang et al. 2008). Spring and autumn appear to be transient periods with IW occurrences of 18 and 11 %, respectively. Such striking seasonal variations can be attributed to a shallower and sharper summertime pycnocline, which favors the IW activity much more than its deeper winter counterpart. Wintertime mixing diffuses the density gradients, and therefore reduces the horizontally propagating IW energy due to weaker generation.

The first reported microstructure measurements near the SCS northern shelf break (St. Laurent 2008) were taken during the late winter-monsoon season, in the background of a deep pycnocline. The IW field observed on the shelf break was more complex than soliton-like depression anomalies observed in other seasons (Orr and Mignerey 2003; Duda et al. 2004; Klymak et al. 2006) and in other regions, such as the Virginia (Nash et al. 2004), New England (e.g., MacKinnon and Gregg 2003, 2005), and Oregon (e.g., Moum et al. 2007) shelves as well as in the European shelf seas (e.g., Rippeth et al. 2005; Inall et al. 2011). A high-amplitude internal wave in SCS near the Dongsha Plateau, which generated density overturn of about 30 m high, with the measured dissipation rate of 10^{-4} W/kg and induced mixing in the pycnocline, was characterized by a diffusivity exceeding 10^{-3} m^2 s^{-1} (St. Laurent et al. 2011). The column-integrated turbulent kinetic energy (TKE) dissipation rate $\widehat{\varepsilon} \approx 50$ mW/m^2 was about an order of magnitude larger than the pure frictional dissipation of local barotropic tide. Note that the integrated dissipation over large areas of SCS could be much higher in the summertime. Because of the observed seasonal variability of IW, the IW-related mixing in SCS is expected to have strong seasonal as well as regional variability. Enhanced mixing in the SCS pycnocline in the vicinity of the Luzon Strait has already been reported by Tian et al. (2009).

In this paper, we study the variability of turbulence in the upper pycnocline of the Luzon Strait, in the central deep basin of the northern SCS, and over a wide shelf along the southeastern coast of China based on the microstructure and accompanying shipboard acoustic Doppler current profiler (ADCP) measurements conducted during the summer seasons of 2009 and 2010. The observations and details of data processing are described in "Observations and data processing" section. The layer-averaged dissipation rates $\langle \varepsilon_p \rangle$ in the upper pycnocline are discussed in "The dissipation rate in the upper pycnocline of the deep basin" section, and the contribution of pycnocline and boundary layers to the integrated dissipation on the shelf is estimated in "Turbulence on the shelf and near the shelf break" section. In "Scaling of TKE dissipation in the pycnocline" section, the mean dissipation in the pycnocline is linked to the Richardson number; a parameterization of $\langle \varepsilon_p \rangle$ suggested by MacKinnon and Gregg (2003) is also evaluated. Discussion and summary of the results are given in "Summary" section.

2 Observations and data processing

The measurements in SCS were conducted in 2009 (July 25–August 13) and 2010 (May 17–21) at the stations shown in Fig. 1 by red and magenta circles, respectively. At across-shelf sections, 24 stations are marked with E, A, and S. In 2010, six stations were taken across the Luzon Strait (LS hereafter) and another eight stations (O1–O8) were located ~30 and 60 mi to the west (see Fig. 1). The maximum depth of each cast was limited by the depth of the ocean floor on the shelf or by the length of a tethered cable in deep waters (usually reaching $z_{max} \approx 160$ m).

As a protocol, three consecutive casts of the MSS-60 profiler (Prandke and Stips 1998) were launched at each station to obtain the burst-averaged profiles of temperature $T(z)$, salinity $S(z)$, potential density $\sigma_\theta(z)$, and the TKE dissipation rate $\varepsilon(z)$. The averaging reduces the short-term variations of stratification and turbulence at various depths (the vertical coordinate z is positive downwards). The interval between individual casts was 3–5 min at shallow stations and 8–10 min at the deeper stations. The MSS-60 carried two parallel airfoil (PNS98) sensors, a fast-response temperature sensor (FP07), three standard CTD sensors, and an accelerometer. The sampling rate for all sensors was 1,024 Hz, thus enabling the measurement of small-scale shear with a vertical resolution of ~6 mm for a typical falling speed of ~0.65 m/s.

The dissipation rate computations followed a well-established methodology (e.g., Stips 2005; Lozovatsky et al. 2005; Roget et al. 2006; Liu et al. 2009). High-amplitude spikes were detected and removed using an iterative procedure. The low-frequency variations of shear signal and the high-frequency noise were then removed by a second-order Butterworth band-pass filter with cut-off frequencies 1 and 100 Hz, corresponding to the wavenumbers $k = 1.5$ and 300 cpm, respectively. The spectral densities of denoised small-scale shear signal of the airfoil probe were fitted with the Nasmyth spectrum at every 1-m segment of the vertical profile, and ε was calculated by integrating those spectra and using a standard isotropic formula $\varepsilon = 7.5\nu(du'/dz)^2$, where ν is the kinematic viscosity of seawater. The noise level of the MSS dissipation estimates is about 10^{-9} W/kg (see the shear spectra in Liu et al. 2009). All sensors of MSS-60 were recalibrated before and after each cruise. The lowest registered level of ε on the shelf and in the upper layer ($z < 160$ m) of deep waters was 7×10^{-9} W/kg, which could be related to high seasonal activity of internal

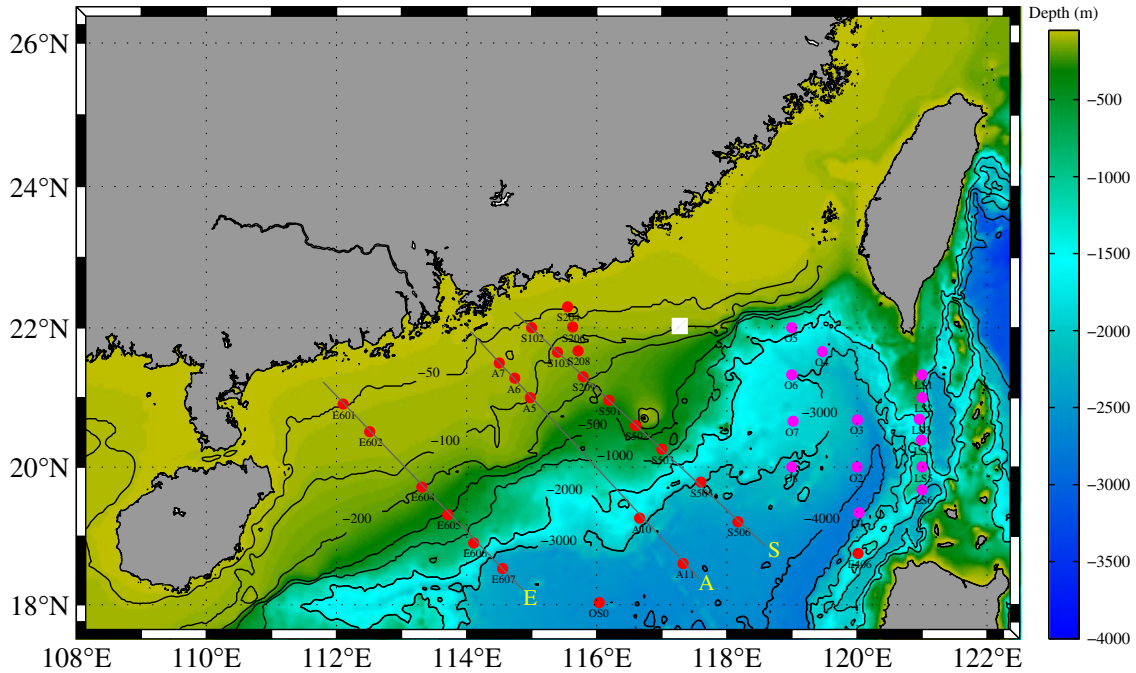

Fig. 1 Stations of the 2009 (*red*) and 2010 (*magenta*) cruises. The *white square* indicates the measurement site of St. Laurent (2008)

waves in the SCS summer pycnocline (Huang et al. 2008); the effect of possible slightly above-average contamination of shear signal by instrument vibration, however, could not be eliminated.

The mean shear, $Sh = \sqrt{(\Delta\widetilde{u}/\Delta z)^2 + (\Delta\widetilde{v}/\Delta z)^2}$, where $\widetilde{u}(z)$ and $\widetilde{v}(z)$ are meridianal and zonal components of mean horizontal velocity, was calculated with $\Delta z = 8$ m due to the limitations of a shipboard 300 kHz ADCP, which was used in the year 2009 cruise. Here, the mean velocity is defined as the initial 1-min averaged ADCP signal, subsequently averaged over the time intervals of MSS measurements (~10 min). The squared buoyancy frequency N^2 was estimated using the reordered potential density profiles at the same segments as those used for Sh and the corresponding Richardson numbers $Ri = N^2/Sh^2$ were calculated. No ADCP data are available for 2010 cruise because of an instrument malfunction.

3 The dissipation rate in the upper pycnocline of the deep basin

A series of $\sigma_\theta(z)$ profiles at the LS transect (Fig. 2a) shows the boundaries of the segments selected for the calculation of averaged dissipation rate in the pycnocline $\langle \varepsilon_p \rangle = \frac{1}{z_{end} - z_i} \int_{z_i}^{z_{end}} \varepsilon(z)\, dz$ between an initial z_i and ending z_{end} depths are shown. The same approach (see the caption of Fig. 2) was used at all other deep-water stations. The individual $\varepsilon(z)$ profiles (examples in Fig. 2b, c) were also employed in the selection process to clarify z_i. The lower boundaries of selected segments z_{end} were identified by the depths where the data deviate from the linear sections of $\sigma_\theta(z)$ profiles.

The thickness of the selected pycnocline segments $h_p = z_{end} - z_i$ varied in deep waters between 67 and 147 m, with 101 m on the average. On the shelf and shelf break, the corresponding numbers are 18, 68, and 34 m and 29, 93, and 70 m, respectively. The boundaries of the selected segments at all stations with $h_p > 18$ m are shown in Fig. 3, along with the estimates of $\langle \varepsilon_p \rangle$ in the pycnocline at each station. The station numbers in this plot are arranged from section E to section S for 2009 transects (shallower stations first), and from the southern stations (O1 and O8) of the most western 2010 transect and LS6 of the LS transect to the most northeastern station LS1 (see Fig. 1).

Note that an individual 1-m averaged dissipation sample $\varepsilon(z_i)$ is estimated with a typical error of 50 % (e.g., Roget et al. 2006). Thus, the error of the mean value $\langle \varepsilon_p \rangle$ calculated over the segments of 67–147 m long should not exceed 4–8 %, allowing statistically robust comparison of $\langle \varepsilon_p \rangle$ at different stations.

Figure 3 shows that the averaged dissipation rate $\langle \varepsilon_p \rangle$ in the pycnocline on the shelf is $(3-6)\times10^{-8}$ W/kg, which is about two to three times lower than that near the shelf break, where $\langle \varepsilon_p \rangle$ went up to 1.7×10^{-7} W/kg. The maximum dissipation $\langle \varepsilon_p \rangle^{max} = 1.3\times10^{-7}$ W/kg in the deep-water pycnocline was observed at LS3 in the center of LS (Figs. 1 and 3), where strong IW are generated (Lien et al. 2005; Klymak et al. 2006; Jan et al. 2008; Alford et al. 2010, 2011). It appeared that the 11 deep-water ($H > 500$ m) stations taken in 2009 mainly to

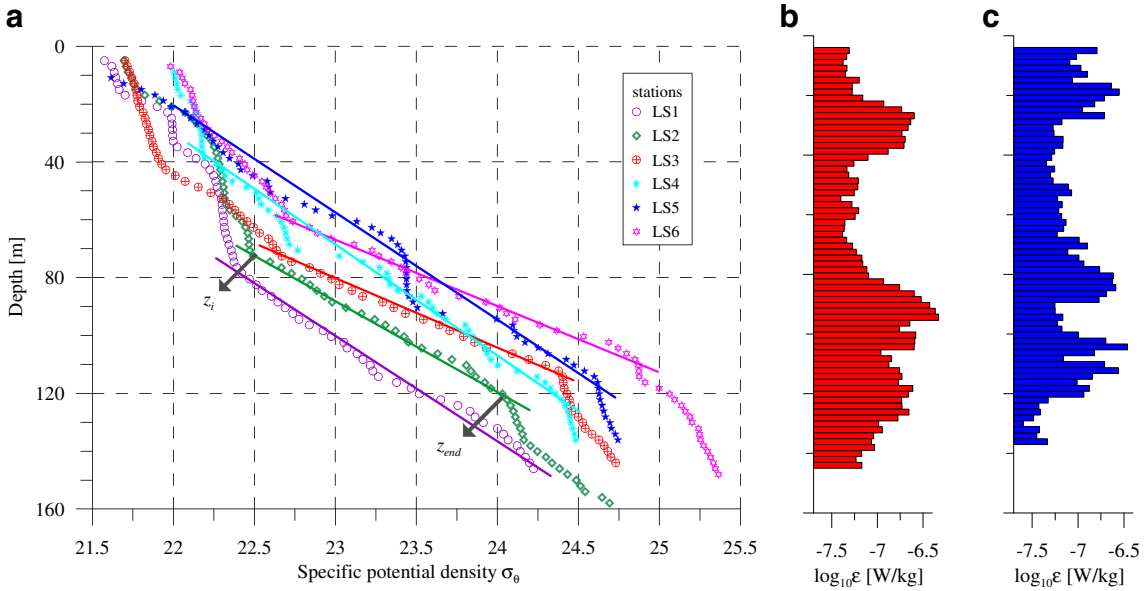

Fig. 2 **a** The potential density profiles across the Luzon Strait from the northern station LS1 to the southern station LS6 (see map in Fig. 1). The *straight lines* show the approximately linear segments of $\sigma_\theta(z)$ in the pycnocline selected for the calculation of $\langle \varepsilon_p \rangle$ at this transect. The upper depths of the segments are specified by the intersection points between the approximations and the data. The upper z_i and lower z_{end} depths for LS2 are shown as an example; **b, c** the dissipation profiles $log_{10}\varepsilon(z)$ at LS3 and LS5, respectively; the depth axes are the same as in (**a**)

the south of $\varphi = 20°$N showed consistently lower level of $\langle \varepsilon_p \rangle$ compared to all the 14-year 2010 stations taken either at or to the north of $\varphi = 20°$N (see also Liu and Lozovatsky 2012). It was hypothesized and later confirmed by in situ measurements (Ramp et al. 2004) and SAR images (Zhao et al. 2004; Zheng et al. 2007; Huang et al. 2008) that the dominant direction of internal wave propagation in the northern SCS is from LS to the west–northwest. The westward propagation of NLIW originated at LS has also been supported by numerical simulations of Shaw et al. (2009) and Buijsman et al. (2010).

Although $\langle \varepsilon_p \rangle$ at each of the 2010 stations is larger than $\langle \varepsilon_p \rangle$ at all but two of the 2009 stations, relatively small number and short duration (less than 1 h at each station) of profiling measurements preclude us of making definitive conclusions about this difference, which could be caused by a variety of factors.

Many large-scale overturns that could locally increase the dissipation rate by an order of magnitude (Liu et al. 2009) or more were missed in our measurements. These powerful events are likely to occur only sporadically (once or twice) during the tidal cycle (see Lee et al. 2006; Liu et al. 2009), but they can substantially elevate the dissipation level in the pycnocline. Extreme-amplitude NLIW are more probable in the northwestern part of the SCS than in the south because of the predominant propagation of NLIW from LS to the west and northwest (Lien et al. 2005; Klymak et al. 2006; Jan et al. 2008; Alford et al. 2010, 2011; Ramp et al. 2010; Cai et al. 2012).

Wind-induced inertial oscillations, which dissipate within the pycnocline, can induce intermittent mixing raising the possibility that $\langle \varepsilon_p \rangle$ variability can be due to the relative phase of inertial oscillations (e.g., Burchard and Rippeth 2009; van der Lee and Umlauf 2011). The phases of inertial oscillations (when/if they exist) are unknown for this data set, but it is highly plausible that they are different at different stations, not biasing the data too much. Some effects of inter-seasonal and tidal (spring-neap) variability can also contribute to the observed spatio-temporal variability of $\langle \varepsilon_p \rangle$ in the northern SCS.

To verify the hypothesis that variations of $\langle \varepsilon_p \rangle$ in the northern SCS are mainly associated with the variations of IW energy, we calculated the available potential energy (APE) of IW per unit mass $P_{IW} = 1/2\psi_p^2 \langle N^2 \rangle_p$ (e.g., Scotti et al. 2006), where ψ_p is a characteristic amplitude of the vertical displacements $\eta(z)$ in the pycnocline, $\psi_p = \mathrm{rms}(\eta)$. Propagating internal waves produce reversible perturbations of density profiles (the so-called wave-induced reversible fine structure) (Fedorov 1978), which can be characterized by the density disturbances $\rho_{fs}(z) = \rho(z) - \widetilde{\rho}(z)$. Dividing ρ_{fs} by the mean density gradient in a selected layer of the pycnocline, $\eta(z)$ was estimated (e.g., Fedorov 1978; Lozovatsky et al. 2003), from which ψ_p and P_{IW} can be calculated. Here, $\widetilde{\rho}(z)$ is a low-pass-filtered density profile. The filter cutoff wavelength that separates the mean and fine-structure (IW-induced) components, $\lambda_{cut} = 8$ m, was chosen following the temperature gradient spectra of Gregg (1977) and the composite shear spectrum of Gargett et al. (1981), where NLIW energy cascade to turbulence occurs at vertical wave numbers $10^{-1} < k < 1$ cpm ($k \sim \eta^{-1}$). A characteristic value of ψ_p, which depends on the choice of λ_{cut}, ranged between 2 and 4 m exceeding 5 m only at a few stations. This eliminates the contribution of high-amplitude ($k << 10^{-1}$ cpm) solitary waves to P_{IW}. As such, P_{IW} should be considered as an approximate estimate of APE of the background internal wave field at each station.

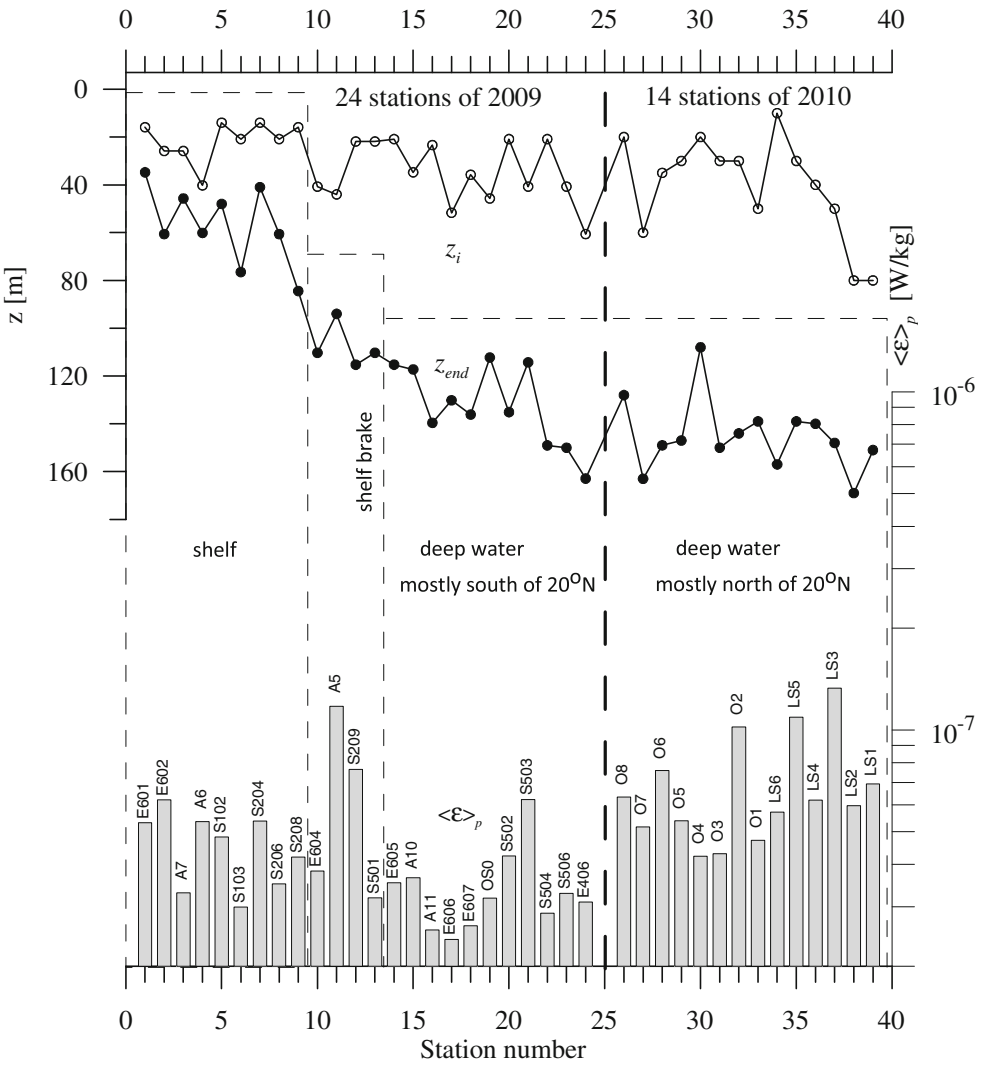

Fig. 3 The averaged dissipation rate $\langle \varepsilon_p \rangle$ (bar chart) in the pycnocline and the upper z_i and lower z_{end} boundaries of the segments selected for calculation of $\langle \varepsilon_p \rangle$. The locations of the shelf (E601–S208), shelf break (E604–S501), and two segments (E605-E406) and (O8-LS1) of deep water stations are shown on the map in Fig. 1

The $\langle \varepsilon_p \rangle$ samples showed a generally increasing trend with P_{IW}, which is presented in Fig. 4, where individual samples of $\langle \varepsilon_p \rangle$ are plotted versus P_{IW} at every station as well as the bin-averaged (over three points along P_{IW}) estimates of the dissipation and APE of IW. It appears that $\langle \varepsilon_p \rangle$ and P_{IW} are reasonably well correlated (r^2=0.72), particularly for bin-averaged samples. The regression can be specified in terms of a background dissipation rate ε_0, P_{IW}, and a characteristic time scale of APE dissipation τ_{APE} as follows:

$$\langle \varepsilon_p \rangle = \varepsilon_0 + P_{IW}/\tau_{APE}, \quad (1)$$

where $\varepsilon_0 = 3.12 \times 10^{-8}$ W/kg (or m^2/s^3) and $\tau_{APE} \approx 5.8$ h. If the total energy of the buoyancy induced internal waves $E_{IW}=(K_{IW}+P_{IW})$ is equally portioned between potential and kinetic K_{IW} energies (Philips 1966), then Eq. (1) suggests that E_{IW} of background IW field in the pycnocline for this case dissipates with a time scale $\tau_{IW}=(K_{IW}+P_{IW})/\langle \varepsilon_p \rangle$ of approximately 12 h, increasing ε_0 proportionally with the IW energy. The background level of the dissipation is relatively high, possibly associated with the dissipation of the kinetic energy of both IW and turbulence generated by various mechanisms

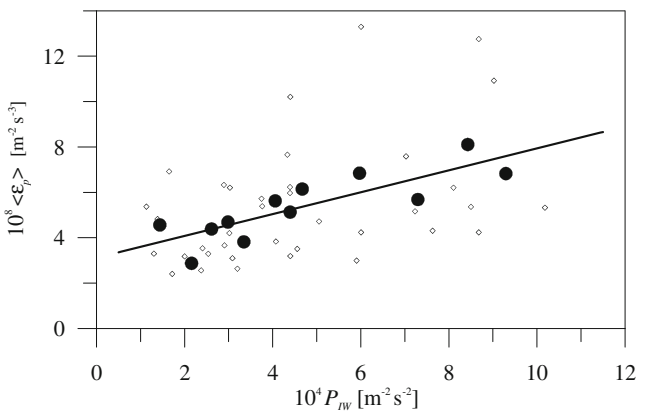

Fig. 4 Averaged dissipation rate in the pycnocline $\langle \varepsilon_p \rangle$ vs. the APE of internal waves P_{IW} at all 38 stations. The *straight line* is a linear regression for bin-averaged (filled) samples. The regression parameters are given in the text

to be discussed in "Scaling of TKE dissipation in the pycnocline" section.

4 Turbulence on the shelf and near the shelf break

Enhanced turbulence at and near the shelf breaks has been observed in many regions (e.g., Inall et al. 2000; Sharples et al. 2001; MacKinnon and Gregg 2003; Carter et al. 2005; Rippeth et al. 2005; Lee et al. 2006; Liu et al. 2009; Schafstall et al. 2010). The only measurements of $\varepsilon(z)$ at the shelf break of SCS have been reported so far by St. Laurent (2008), St. Laurent et al. (2011) and Liu and Lozovatsky (2012). In our study, the estimates of the averaged dissipation $\langle \varepsilon_p \rangle$ on the shelf were obtained between the well-defined upper boundary of BBL and the lower boundary of the surface mixed layer h_{SL} (examples are given in Fig. 5). In addition, the depth-integrated dissipation rate $\widehat{\varepsilon}_p = \int_{z_i}^{z_{end}} \rho\varepsilon(z)dz$, where ρ is the water density, was calculated in the pycnocline and in BBL.

4.1 Geometry of SL, BBL, and pycnocline

To estimate the relative contributions of three major layers to the depth-integrated dissipation on the shelf, the thicknesses of BBL, pycnocline, and SL as well as the fractions of the entire water column occupied by these layers were analyzed first. Figure 6a shows that the characteristic height of BBL is about 10 m (max h_{BBL}=27 m), the mean and median depths of SL are 14 and 8 m (max h_{SL}=44 m), and the corresponding numbers for the thickness of the pycnocline h_p are 29 and 22 m. The fractions of the water column occupied by BBL, pycnocline, and SL (Fig. 6b), on the average, are 0.23, 0.53,

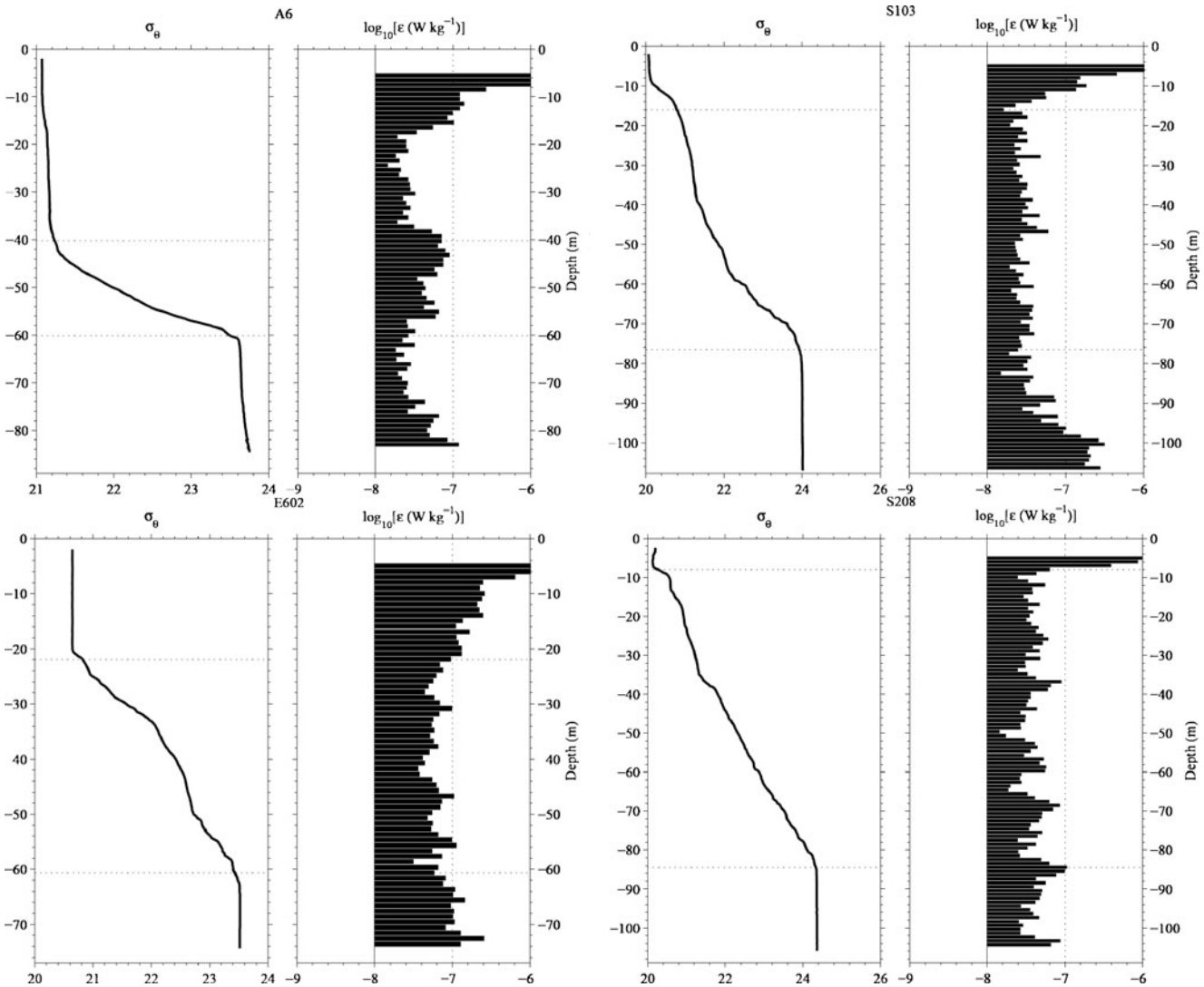

Fig. 5 Examples of the potential specific density and the dissipation rate profiles on several shelf stations. The *dotted lines* show the upper and lower boundaries of the pycnocline segments selected for calculation of $\langle \varepsilon_p \rangle$

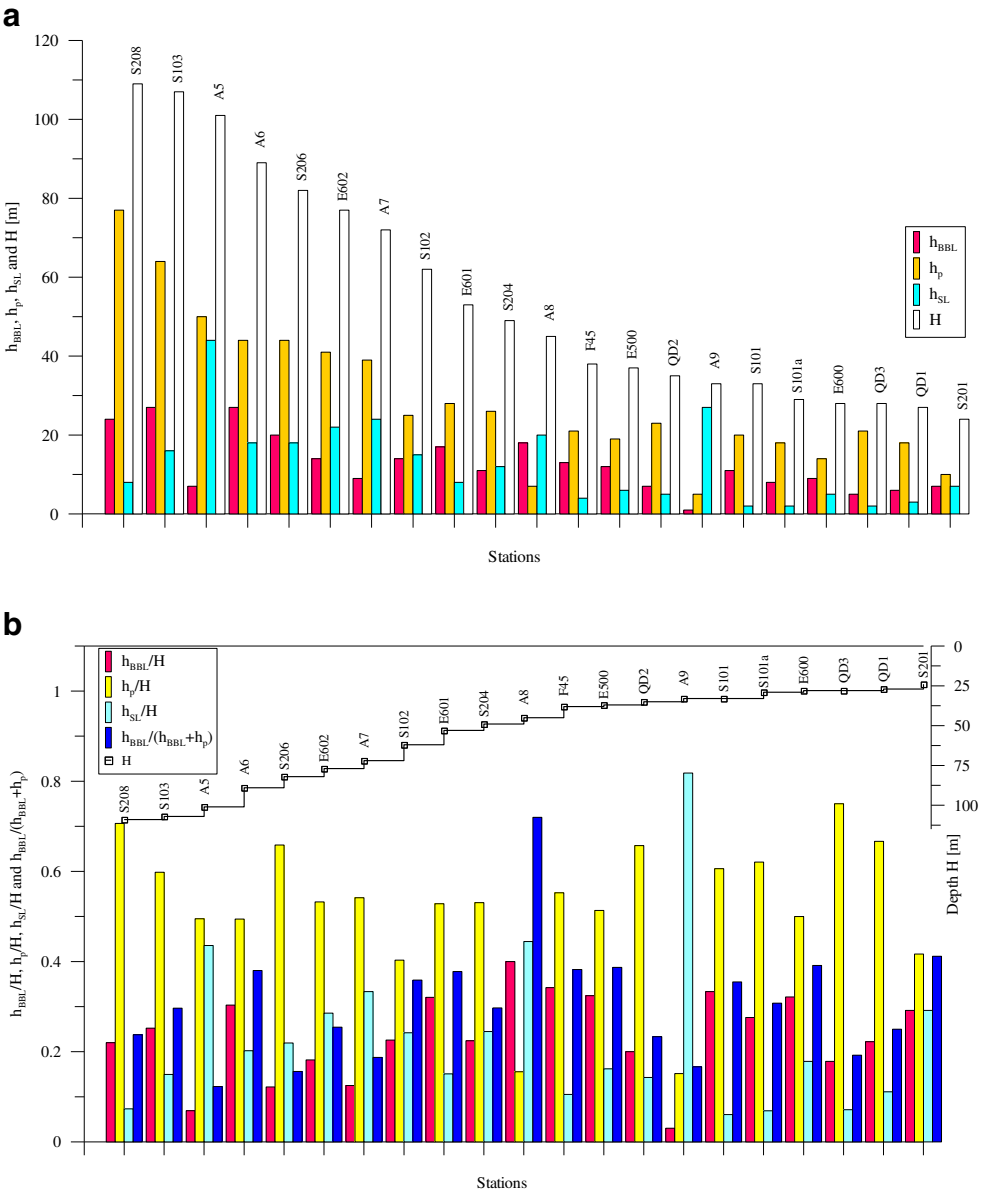

Fig. 6 Thicknesses of the BBL, pycnocline, and SL on the shelf (**a**) and the fractions of the water column (**b**) occupied by these layers (*bars*). The station names are given above the *stepped line* that shows the depth H of the seafloor (right axis). The data in the plot are arranged from the deeper to shallower stations

and 0.24, respectively. The variation coefficient (*rms*/mean) is smallest (0.28) for the ratio h_p/H; larger (0.43) for h_{BBL}/H; and the largest (0.76) for h_{SL}/H. The latter reflects the fact that the depth of SL across the shelf is constantly affected by variable sea-surface fluxes but not the water depth. On the shelf, the pycnocline thickness h_p is reasonably well correlated with the water depth H (see the regression statistics in Fig. 7). This is not the case for h_{BBL} and more so for h_{SL}. Although a linear regression of h_p vs. H holds for the complete set of shelf stations [with slightly different compared to Fig. 7 regression coefficient (0.55) and a lower r^2=0.86], we have limited our further analysis to 10 relatively deep stations (H>50 m) with a fairly wide pycnocline (h_p>18 m) to ensure statistical reliability of integrated estimates of $\widehat{\varepsilon}$ and other variables in BBL and pycnocline. The samples from these

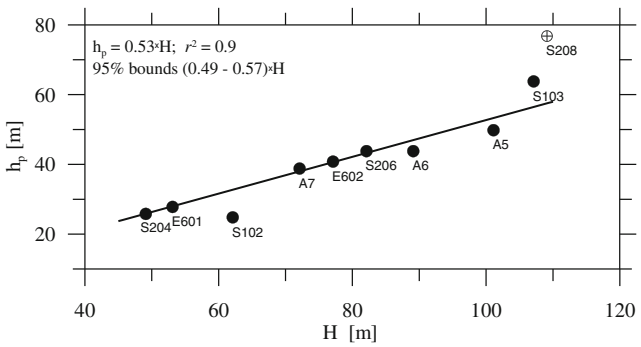

Fig. 7 Thickness of the pycnocline h_p vs. the seafloor depth H at 10 shelf stations with H >50 m and h_p >18 m. A linear regression with the 95 % confidence bounds and the coefficient of determination r^2 are given in the plot, not accounting for St. 208, which appears to be an anomaly

stations are shown in Fig. 7. The observed correspondence between h_p and H could be linked to smaller phase speeds and group velocities of high-amplitude IW in shallower waters compared to the deep ocean. The lower energy density in the stratified interior reduces the potential for turbulence and mixing that is responsible for widening of the pycnocline.

The positive correlation between the pycnocline thickness and a characteristic bulk buoyancy scale $\widetilde{L}_b = \widetilde{\varepsilon}_p^{1/3}/\langle N \rangle_p$ (Fig. 8) supports the assumption that h_p is predominantly influenced by internal mixing in the pycnocline rather than by turbulence in the surrounding boundary layers (Turner 1973). Here, $\widetilde{\varepsilon}_p = \widehat{\varepsilon}_p/\rho$. In nine out of ten shelf stations, h_p shows a growing trend with $\widetilde{L}_b$. It appears that at St. A5 the pycnocline was eroded by strong wind-induced mixing that caused deepening of SL to more than 40 m, therefore reducing h_p. Simultaneously, an elevated dissipation rate was registered in the pycnocline at A5.

4.2 Integrated dissipation on the shelf

The depth-integrated dissipation rate $\widehat{\varepsilon}_p$ in the pycnocline is a function not only of $\varepsilon(z)$ but also of the integration range (z_{end}–z_i), which cannot be firmly specified in deep waters. On the shelf, however, the upper and lower boundaries of the pycnocline sandwiched between SL and BBL are usually well defined (see Fig. 5), thus making the depth-integrated dissipation rate $\widehat{\varepsilon}_p$ a representative measure of the turbulence intensity in stratified interior.

The estimates of dissipation rate integrated over the thickness of SL $\widehat{\varepsilon}_{SL}$, pycnocline $\widehat{\varepsilon}_p$, and BBL $\widehat{\varepsilon}_{BBL}$ at selected shelf stations are shown in Fig. 9 (stacked bars), along with the ocean depth and the BBL thickness. The relative contribution $R_\varepsilon = \widehat{\varepsilon}_{BBL}/\left(\widehat{\varepsilon}_{BBL} + \widehat{\varepsilon}_p\right)$ of $\widehat{\varepsilon}_{BBL}$ to the total depth-integrated dissipation in the water interior (excluding SL) is in Table 1. Note that $\widehat{\varepsilon}_{BBL}$ was estimated by extrapolating $\varepsilon(z)$ profiles from the cast end point down to the seafloor (specifically to 0.05 m above the bottom) using the law-of-the-wall (LofW) formula $\varepsilon(H-z)=u_*^3/\kappa(H-z)$ for the lower 2–3 m of the water column ($\kappa=0.4$ is the von Karman constant). The corresponding estimates for the friction velocity u_* are given in Table 1. The applicability of LofW in a well-mixed near-bottom turbulent layer have been reported for the East China Sea (Lozovatsky et al. 2008a, b, 2012) and other regions (e.g., Simpson et al. 1996; Lueck and Lu 1997; Sanford and Lien 1999; Moum and Nash 2000; Elliott 2002; Perlin et al. 2005; Umlauf and Arneborg 2009; van der Lee and Umlauf 2011).

Note that $\widehat{\varepsilon}_{SL}$ is overwhelmingly affected by wind mixing, varying from ~0.3 mW/m^2 (S204) to 14.9 mW/m^2 (E602). The fraction of the dissipation in SL (excluding upper 5 m) is as low as 9 % and as high as 70 % of that over the entire water column. Our focus, however, is on the pycnocline and BBL, while $\widehat{\varepsilon}_{SL}$ is presented here only for completeness.

As shown in Fig. 9 and Table 1, $\widehat{\varepsilon}_{BBL}$ on the shelf dominates over the integrated dissipation in the pycnocline $\widehat{\varepsilon}_p$. The absolute values of $\widehat{\varepsilon}_{BBL}$ vary from 3.7 (S206) to 18.7 (S102) mW/m^2. Except at St. A5, $\widehat{\varepsilon}_{BBL}$ takes more than 70 % of the combined dissipation $\left(\widehat{\varepsilon}_{BBL} + \widehat{\varepsilon}_p\right)$, but often it is close to 90 %. Only at St. A5, $\widehat{\varepsilon}_{BBL}$ is equal to $\widehat{\varepsilon}_p$, because of

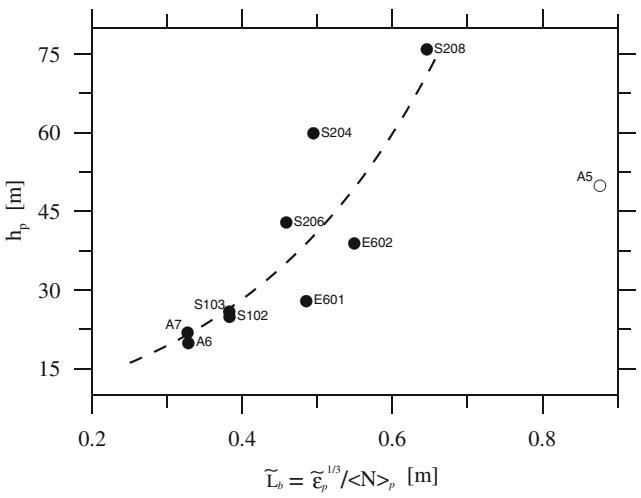

Fig. 8 The pycnocline thickness h_p vs. the bulk buoyancy scale $\widetilde{L}_b$ at selected shelf stations. The *dashed line* is a least squared approximation of all samples excluding A5

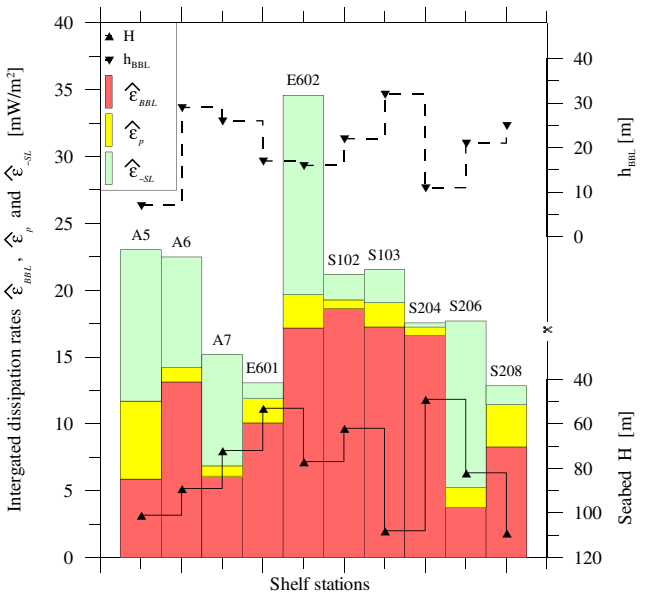

Fig. 9 The integrated dissipation rates at shelf stations (A5, … S208) in the pycnocline $\widehat{\varepsilon}_p$ and SL $\widehat{\varepsilon}_{SL}$ (excluding upper 5 m). They are stacked over the integrated dissipation in BBL $\widehat{\varepsilon}_{BBL}$. A combined height of the three bars at every station gives the total integrated dissipation of the water column below $z=5$ m. The depth of the seabed H and the height of BBL h_{BBL} are also shown in the plot

Table 1 The estimates of friction velocity u_* for selected shelf stations based on extrapolation of $\varepsilon(z)$ profiles down to the seabed using the law-of-the-wall model

Station	$u_* \times 10^3$, m/s	$R_\varepsilon = \widehat{\varepsilon}_{BBL}/(\widehat{\varepsilon}_{BBL} + \widehat{\varepsilon}_p)$
A5	4.72	0.50
A6	6.01	0.92
A7	4.58	0.89
E601	5.54	0.84
E602	6.61	0.87
S102	6.72	0.97
S103	6.52	0.91
S204	6.56	0.96
S206	3.89	0.71
S208	5.14	0.72

The fraction R_ε of the integrated dissipation rate in BBL $\widehat{\varepsilon}_{BBL}$ compared to the total dissipation in BBL and pycnocline $(\widehat{\varepsilon}_{BBL} + \widehat{\varepsilon}_p)$ is also given

an unusual stratification conditions. It has very deep SL (h_{SL}=44 m), very shallow BBL (h_{BBL}=7 m), and a wide, highly turbulent pycnocline (h_p=50 m). Among all shelf stations, the mean dissipation in the pycnocline at A5 shows the highest, $\langle\varepsilon_p\rangle = 1.18\times10^{-7}$ W/kg (see Fig. 3). The dissipation measurements at A5 may have coincided with a turbulent event akin to the propagation of a solitary wave or a packet of NLIW generated at the shelf break in close proximity to A5 (Fig. 1). Although $\widehat{\varepsilon}_{BBL}$ is the major contributor to the depth-integrated dissipation on the shelf away from the shelf break, it appears that baroclinic motions, such as internal tidal waves, have only little influence on $\widehat{\varepsilon}_{BBL}$, given that $\widehat{\varepsilon}_{BBL}$ is generally consistent with the dissipation estimates for barotropic tide.

The magnitude V_{td} of tidal currents near the seafloor on the shelf (~7–10 m above the bottom) varies between ~0.05–0.10 and 0.15–0.2 m/s based on our ADCP data. The usual parameterization for the tidal dissipation in BBL, $\varepsilon_{td} \sim \rho C_D |V_{td}| V_{td}^2$, where the drag coefficient $C_D = 2.5\times10^{-3}$ (which may vary during the tidal cycle; Lozovatsky et al. 2008b), could be as low as 0.3–2.5 mW/m^2 and as high as 9–20 mW/m^2; $\widehat{\varepsilon}_{BBL}$ = 3.7–18.7 mW/m^2 is well inside this range (see Fig. 9).

The integrated dissipation rate in the lower 10 m of the water column at the shelf break (H=160 m) to the north of our stations (see Fig. 1) has been estimated as 25 mW/m^2 (St. Laurent 2008). By comparing this number with ε_{td} calculated for an assumed V_{td}=0.1 m/s, St. Laurent (2008) inferred that the observed high dissipation is related to baroclinic energy. We note, however, that $\varepsilon_{td} \sim V_{td}^3$, and V_{td} can easily go up to 0.2 m/s or above (e.g., Souza and Howarth 2005; Lozovatsky et al. 2010). Thus, the high level of integrated dissipation in BBL can be explained by pure bottom drag of barotropic flow although the impact of baroclinic energy may exist, being sometime comparable with ε_{td} (see also Inall et al. 2000).

5 Scaling of TKE dissipation in the pycnocline

In the pycnocline of SCS, the dissipation is expected to be affected by packets of propagating internal waves as well as by shear instability of mean currents, inertial oscillations, and tidal internal waves. Therefore, it is useful to explore parameterization of $\langle\varepsilon_p\rangle$ in terms of N^2 and vertical shear Sh of low frequency motions or the conventional gradient Richardson number $Ri = N^2/Sh^2$. The TKE dissipation is expected to decrease with suppression of turbulence at high Ri.

Analyzing the possible dependence of dissipation rate in SCS on the Richardson number, we employed only the year 2009 data since the shipboard ADCP failed during 2010 cruise ("Observations and data processing" section). The total number of the available shear estimates $\overline{Sh}$ (vertical spacing Δz = 8 m) is 152. The corresponding $\overline{N}$ and $\overline{\varepsilon}$ for this analysis were also calculated over the same 8-m layers. The individual and bin-averaged samples of $\overline{\varepsilon}$ are plotted in Fig. 10 against $Ri = \overline{N}^2/\overline{Sh}^2$. The data show a decreasing tendency of dissipation with increasing Ri, but the scatter is large. This tendency is much clearer for the bin-averaged data (10 samples in the bin). It can be approximated by the formula

$$\overline{\varepsilon} = \varepsilon_0 + \frac{\varepsilon_m}{(1 + Ri/Ri_{cr})^{1/2}}, \tag{2}$$

developed in the spirit of Munk and Anderson (1948); see also Lozovatsky et al. (2006). Here, $\varepsilon_0 = 2.2\times10^{-8}$ W/kg is a relatively high background dissipation (similar to $\varepsilon_0 = 3.12\times10^{-8}$ in Eq. 1), which is not affected by shear instability at scales larger than 8 m, but probably sustained by smaller scales processes. In weakly stratified layers ($Ri \ll Ri_{cr}$), where Ri_{cr}=0.25 is a critical Richardson number, the maximum dissipation ($\varepsilon_0 + \varepsilon_m$) is expected with $\varepsilon_m = 7.8\times10^{-8}$ W/kg. The Eq. (2) fits the data with a reasonable coefficient of determination (r^2=0.7); note that 95 % confidence boundaries in Fig. 10 encompass not only the averaged but almost all individual samples. The dependence of $\overline{\varepsilon}$ on Ri is relatively weak ($\sim Ri^{-1/2}$ for $Ri \gg Ri_{cr}$), which could reflect the dual role of N in suppressing and enhancing turbulence via different mechanisms.

In the presence of internal waves, higher APE values of IW are associated with larger N^2 (see "The dissipation rate in the upper pycnocline of the deep basin" section) and strain (e.g., Wijesekera et al. 1993; Alford and Pinkel 2000), which may lead to an enhancement of $\langle\varepsilon_p\rangle$. In addition, local shear of IWs can enhance the production of TKE by superimposing on the mean shear (Woods 1968). Thus, in this case, a product $N \times Sh$ may show a positive correlation with ε, which has been

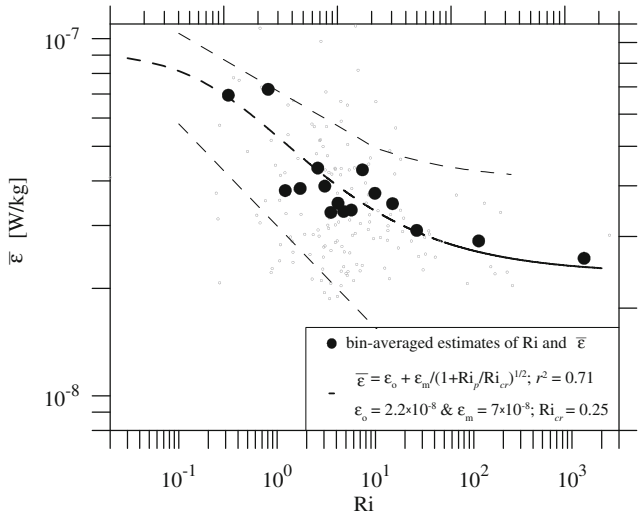

Fig. 10 Original (*small open symbols*) and bin-averaged samples (*large filled symbols*) of the dissipation vs. The Richardson number for all stations of 2009 cruise. The *bold dashed line* is the approximation $\bar{\varepsilon}(Ri)$ given in the legend; the *thin dashed lines* are 95 % confidence boundaries

explored in numerous publications (e.g., Henyey et al. 1986; Gregg 1989; Polzin et al. 1995; MacKinnon and Gregg 2003, 2005; Carter et al. 2005; Schafstall et al. 2010; van der Lee and Umlauf 2011).

In the following, we tested the oft-used parameterization of MacKinnon and Gregg (2003)

$$\varepsilon_{\mathrm{MG}} = \varepsilon_0 (N/N_0) \times (Sh/Sh_0), \tag{3}$$

which is most appropriate for our data set. The values of $N_0 = Sh_0 = 3$ cph and $\varepsilon_0 = 6.9\times10^{-10}$ W/kg were derived by Henyey et al. (1986) from an analytical model (and used by MacKinnon and Gregg 2003), but in later works alternative values of N_0, Sh_0, and ε_0 have been utilized as adjustable parameters. Although the functional dependence $\varepsilon(N,Sh)$ given by Eq. (3) has been mostly supported by measurements from a variety of regions, the variability of ε_0 spans over two orders of magnitude (from ~10^{-10} to more than 10^{-8} W/kg). In MacKinnon and Gregg (2005), $\varepsilon_0 = 1.1\times10^{-9}$ W/kg (New England shelf), while Palmer et al. (2008) and Liu (2010) came up with much larger $\varepsilon_0 = (1.5-1.75)\times10^{-8}$ W/kg analyzing measurements in tidally affected shelf seas west of Britain. Sundfjord et al. (2007) and Schafstall et al. (2010) have reported ε_0 exceeding 10^{-8} W/kg for deep ocean measurements taken close to solid boundaries (e.g., ice edge and continental slope). Substantially smaller $\varepsilon_0 = (1.5-1.7)\times10^{-10}$ W/kg has been assigned by van der Lee and Umlauf (2011) for turbulence influenced by inertial oscillations in the non-tidal Baltic Sea. It appears that ε_0 experiences more regional than temporal variability, as evident from the measurements of MacKinnon and Gregg (2003, 2005) and van der Lee and Umlauf (2011) taken at the same places (New England shelf and Baltic Sea, respectively) but during different seasons, which points to the importance of large- and mesoscale dynamics (influenced by bathymetry and climate) on setting up and maintaining the background levels of IW-induced turbulent dissipation ε_0.

Our data are shown in Fig. 11, where the pycnocline averaged dissipation $\langle\varepsilon_p\rangle$ is plotted against $\varepsilon_{\mathrm{MG}}$ (Eq. 3), which was calculated using the bulk estimates of $\langle N_p\rangle$ and $\langle Sh_p\rangle$ averaged over the same selected segments of pycnocline as $\langle\varepsilon_p\rangle$. The standard $N_0 = Sh_0 = 3$ cph was used, and ε_0 could be as low as 1×10^{-8} and as high as 2×10^{-8} W/kg, yielding the best match to $\langle\varepsilon_p\rangle = \varepsilon_{\mathrm{MG}}$ with $\varepsilon_0 = 1.5\times10^{-8}$ W/kg. The scatter in Fig. 11 is large; however, for $\varepsilon_p < \sim10^{-7}$ W/kg the parameterization (3) is mainly consistent with the data. This indicates the complex nature of the dissipation field in the SCS pycnocline away from LS. A relatively high ($\varepsilon_0 \sim 10^{-8}$ W/kg) background level of viscous dissipation is sustained by the higher energy of the IW field, but episodic large dissipations can also be produced by solitary waves generated at the shelf break and local K-H instabilities of mean currents, which may cause (3) to be invalid.

6 Summary

The variability of the dissipation rate of turbulent kinetic energy and the available potential energy of internal waves have been analyzed for the upper pycnocline of the northern SCS, which includes the Luzon Strait (LS), the central basin, and a wide continental shelf of China.

Near the shelf break, the averaged dissipation $\langle\varepsilon_p\rangle$ was as high as 3×10^{-7} W/kg, which is several times larger than in the pycnocline on the shelf where $\langle\varepsilon_p\rangle = (3-6)\times10^{-8}$ W/kg. This is consistent with the findings of other authors who linked

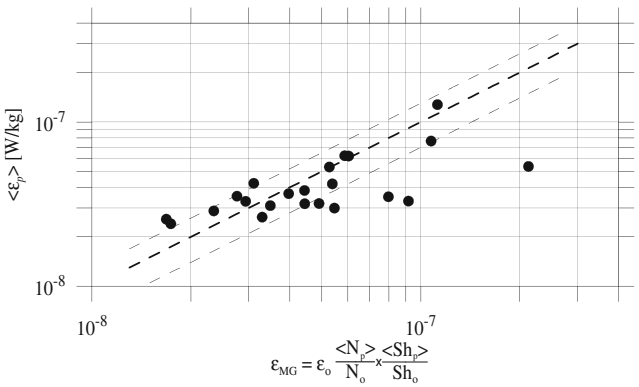

Fig. 11 The averaged dissipation rate in the pycnocline $\langle\varepsilon_p\rangle$ as a function of the dissipation parameterization $\varepsilon_{\mathrm{MG}}$ (McKinnon and Gregg 2003) for the 2009 dataset. The *heavy dashed line* is for $\langle\varepsilon_p\rangle = \varepsilon_{\mathrm{MG}}$ with $\varepsilon_0 = 1.5\times10^{-8}$ W/kg, the upper and lower bounds are for $\varepsilon_0 = 2\times10^{-8}$ W/kg and $\varepsilon_0 = 1\times10^{-8}$ W/kg, respectively. Here $<N_p>$ and $<Sh_p>$ are the averaged buoyancy frequency and the low frequency shear; $N_0 = Sh_0 = 3$ cph

enhancement of turbulence in the pycnocline near the shelf breaks to the generation of nonlinear internal waves therein.

It is hypothesized that the lower values of $\langle \varepsilon_p \rangle$ in the upper pycnocline at the deep stations of 2009 compared to the year 2010 campaign could be attributed mostly to the degeneration of internal waves originated in LS and propagated predominantly to the west–northwest, but a variety of factors (i.e., inertial oscillations, seasonal and tidal cycle variability, etc.) may contribute to the observed disparity. A positive linear correlation between $\langle \varepsilon_p \rangle$ and the available potential energy of the background internal waves P_{IW} in the same layers is in line with hypothesis. A characteristic dissipation time $\tau_{IW}=(K_{IW}+P_{IW})/\langle \varepsilon_p \rangle$ appears to be close to 12 h.

On the western shelf of SCS, it was possible to analyze not only the averaged $\langle \varepsilon_p \rangle$ but also the depth-integrated $\widehat{\varepsilon}$ dissipation in easily identifiable boundary layers (BBL and SL) and in the entire pycnocline bounded by these layers. As expected, the dissipation in SL was governed by the surface fluxes and therefore varied over a wide range depending on weather conditions. On the average, the fractions of water column occupied by SL, pycnocline, and BBL appeared to be 0.23, 0.53, and 0.24, respectively. The pycnocline thickness h_p correlated well with the bulk buoyancy scale $\widetilde{L}_b = \widetilde{\varepsilon}_p^{1/3}/\langle N \rangle_p$, suggesting that h_p was mainly controlled by internal mixing in the pycnocline rather than by turbulence in SL and BBL. The integrated pycnocline dissipation $\widehat{\varepsilon}_p = \int_{z_i}^{z_{end}} \rho\varepsilon(z)dz$, however, contributed only 10–30 % to the total dissipation in the water interior below SL, although we observed an episode where the total dissipation of 12 mW/m^2 was equally partitioned between $\widehat{\varepsilon}_p$ and $\widehat{\varepsilon}_{BBL}$. The dominant fraction of tidal energy on the SCS shelf dissipated within 10–30 m above the bottom, where $\widehat{\varepsilon}_{BBL}$ was as high as 17–19 mW/m^2.

In order to analyze the dependence of dissipation rate on the Richardson number Ri, the estimates of $\overline{\varepsilon}$, $\overline{N}$, $\overline{Sh}$, and therefore Ri were obtained with 8 m vertical resolution. The data of 152 individual samples exhibited a decreasing trend of $\overline{\varepsilon}$ with Ri; this tendency became much clearer in bin-averaged estimates (10 samples per bin). It was parameterized using a formula that account for a relatively weak dependence of $\overline{\varepsilon}$ on Ri ($\sim Ri^{-1/2}$ at high Ri). As such, a dual role of $\overline{N}$ was suggested due to substantial activity of larger-scale internal waves in the region. This mechanism was checked using the MacKinnon–Gregg scaling (3) for the pycnocline averaged dissipations $\langle \varepsilon_p \rangle$ and corresponding $\langle N_p \rangle$ and $\langle Sh_p \rangle$. It appears that for $\varepsilon_p < \sim 10^{-7}$ W/kg, MacKinnon–Gregg formula is generally consistent with our data (Fig. 11) but with $\varepsilon_0=(1-2)\times 10^{-8}$ W/kg, which is much larger than that originally employed by MacKinnon and Gregg (2003, 2005) and reported by van der Lee and Umlauf (2011), but consistent with the estimates of ε_0 given in Palmer et al. (2008), Sundfjord et al. (2007), Liu (2010), and Schafstall et al. (2010). It is suggested that in the pycnocline of SCS away from LS, a relatively high ($\sim 10^{-8}$ W/kg) background level of turbulence is generated by sustained internal-wave energy, which is linked to strong internal tide. The episodic large values of $\langle \varepsilon_p \rangle$ are associated with alternative processes, such as solitary waves generated at the shelf break and the shear of mean currents (Cai et al. 2012).

It seems that the main difference between the studies that showed small and large values of ε_0 is related to the main mechanism of the generation of IW field. In case of van der Lee and Umlauf (2011) (small $\varepsilon_0 \sim 10^{-10}$ W/kg), the IW forcing was associated with wind-induced near inertial oscillations whereas other studies, including the present one (large $\varepsilon_0 \sim 10^{-8}$ W/kg), indicate that the main forcing for IW as the interaction of internal tide with solid boundaries (mainly the shelf break and continental slope). The verification of this hypothesis requires further multi-scale measurements under carefully documented background conditions.

Acknowledgments We are thankful to the research team of Xiamen University and crew of the research vessels who made possible running the field campaigns and conducting microstructure measurements in SCS. The field measurements were funded by the State Key Laboratory of Marine Environmental Science (Xiamen University) and the National Basic Research Program of China (projects 2009CB421200 and 2007CB411803). The analysis presented in this paper was supported by the US Office of Naval Research (grant N00014-05-1-0245), the National Natural Science Foundation of China (grant 41006017), and the Fundamental Research Funds for the Central Universities of China (grant 2010121030).

References

Alford M, Pinkel R (2000) Observations of overturning in the thermocline: the context of ocean mixing. J Phys Oceanogr 30:805–832

Alford MH, Lien R-C, Simmons H, Klymak J, Ramp S, Yang YJ, Tang D, Chang M-H (2010) Speed and evolution of nonlinear internal waves transiting the South China Sea. J Phys Oceanogr 40:1338–1355

Alford MH, MacKinnon JA, Nash JD, Simmons H, Pickering A, Klymak JM, Pinkel R, Sun O, Rainville L, Musgrave R, Beitzel T, Fu K-H, Lu C-W (2011) Energy flux and dissipation in Luzon strait: two tales of two ridges. J Phys Oceanogr 41:2211–2222

Beardsley RC, Duda TF, Lynch JF, Irish JD, Ramp SR, Chiu C-S, Tang TY, Yang Y-J, Fang G (2004) Barotropic tide in the Northeast South China Sea. IEEE J Oceanic Eng 29:1075–1086

Buijsman MC, Kanarska Y, McWilliams JC (2010) On the generation and evolution of nonlinear internal waves in the South China Sea. J Geophys Res 115:C02012. doi:10.1029/2009JC005275

Burchard H, Rippeth TP (2009) Generation of bulk shear spikes in shallow stratified tidal seas. J Phys Oceanogr 39:969–985

Cai S, Xie J, He J (2012) An overview of internal solitary waves in the South China Sea. Surv Geophys 33:927–943

Carter GS, Gregg MC, Lien RC (2005) Internal waves, solitary like waves, and mixing on the Monterey Bay shelf. Cont Shelf Res 25:1499–1520

Chang M-H, Lien R-C, Tang TY, D'Asaro EA, Yang YJ (2006) Energy flux of nonlinear internal waves in northern South China Sea. Geophys Res Lett 33, L03607. doi:10.1029/2005GL025196

Duda TF, Rainville L (2008) Diurnal and semidiurnal internal tide energy flux at a continental slope in the South China Sea. J Geophys Res 113, C03025. doi:10.1029/2007JC004418

Duda TF, Lynch JF, Irish JD, Beardsley RC, Ramp SR, Chiu C-S, Tang T-Y, Yang Y-J (2004) Internal tide and nonlinear internal wave behavior at the continental slope in the northern South China Sea. IEEE J Oceanic Eng 29:1105–1130

Elliottt AJ (2002) The boundary layer character of tidal currents in the Eastern Irish Sea. Estuar Coast Shelf Sci 55:465–480

Farmer DM, Alford MH, Lien R-C, Yang YJ, Chang M-H, Li Q (2011) From Luzon Strait to Dongsha Plateau: stages in the life of an internal wave. Oceanography 24:64–77

Fedorov KN (1978) Thermohaline fine structure of the ocean. Pergamon, Oxford, p 179

Gargett AE, Hendricks PJ, Sanford TB, Osborn TR, Williams AJ (1981) A composite spectrum of vertical shear in the upper ocean. J Phys Oceanogr 11:1258–1271

Gawarkiewicz G, Wang J, Caruso M, Ramp SR, Brink K, Bahr F (2004) Shelf break circulation and thermohaline structure in the northern South China Sea: contrasting spring conditions in 2000 and 2001. IEEE J Oceanic Eng 29:1131–1143

Gregg MC (1977) Variations in the intensity of small-scale mixing in the main thermocline. J Phys Oceanogr 7:436–454

Gregg MC (1989) Scaling turbulent dissipation in the thermocline. J Geophys Res 94:9686–9698

Henyey FS, Wright J, Flatte SM (1986) Energy and action flow through the internal wave field. J Geophys Res 91:8487–8495

Hsu MK, Liu AK, Lin C (2000) A study of internal waves in the China Seas and Yellow Sea using SAR. Cont Shelf Res 20:389–410

Huang W, Johannessen J, Alpers W, Yang J, Gan X (2008) Spatial and temporal variations of internal waves in the northern South China Sea. 2nd International Workshop on advances in SAR oceanography from ENVISAT and ERC missions. January 21–25, Frascati—Rome, Italy

Inall M, Rippeth T, Sherwin T (2000) Impact of nonlinear waves on the dissipation of internal tidal energy at a shelf break. J Geophys Res 105:8687–8705

Inall M, Aleynik D, Boyd T, Palmer M, Sharples J (2011) Internal tide coherence and decay over a wide shelf sea. Geophys Res Lett 38, L23607. doi:10.1029/2011GL049943

Jan S, Lien R-C, Ting C-H (2008) Numerical study of baroclinic tides in Luzon Strait. J Oceanogr 64:789–802

Klymak JM, Pinkel R, Liu C-T, Liu AK, David L (2006) Prototypical solitons in the South China Sea. Geophys Res Lett 33, L11607. doi:10.1029/2006GL025932

Lee J-H, Lozovatsky ID, Jang S-T, Jang C-J, Hong C-S, Fernando HJS (2006) Episodes of nonlinear internal waves in the Northern East China Sea. Geophys Res Lett 33, L18601. doi:10.1029/2006GL027136

Li Q, Farmer DM (2011) The generation and evolution of nonlinear internal waves in the deep basin of the South China Sea. J Phys Oceanogr 41:1345–1363

Liang NK, Liu AK, Peng CY (1995) A preliminary study of SAR imagery on Taiwan coastal water. Acta Oceanogr Taiwanica 34:17–28

Lien R-C, Tang TY, Chang MH, D'Asaro EA (2005) Energy of nonlinear internal waves in the South China Sea. Geophys Res Lett 32, L05615. doi:10.1029/2004GL022012

Liu Z (2010) Instability of baroclinic tidal flow in a stratified fjord. J Phys Oceanogr 40:139–154

Liu AK, Hsu MK (2004) Internal wave study in the South China Sea using Synthetic Aperture Radar (SAR). Int J Remote Sens 25:1261–1264

Liu Z, Lozovatsky ID (2012) Upper pycnocline turbulence in the northern South China Sea. Chinese Sci Bull 57:2302–2306. doi:10.1007/s11434-012-5137-8

Liu Z, Wei H, Lozovatsky ID, Fernando HJS (2009) Late summer stratification and turbulence in the Yellow Sea. J Mar Syst 75:459–472

Lozovatsky ID, Morozov EG, Fernando HJS (2003) Spatial decay of energy density of tidal internal waves. J Geophys Res 108, C63201. doi:10.1029/2001JC001169

Lozovatsky I, Figueroa M, Roget E, Fernando HJS, Shapovalov S (2005) Observations and scaling of the upper mixed layer in the North Atlantic. J Geophys Res 110, C05013. doi:10.1029/2004JC002708

Lozovatsky ID, Roget E, Fernando HJS, Figueroa M, Shapovalov S (2006) Sheared turbulence in a weakly-stratified upper ocean. Deep Sea Res I 53:387–407

Lozovatsky ID, Liu Z, Hao W, Fernando HJS (2008a) Tides and mixing in the northwestern East China Sea. Part I: rotating and reversing tidal flows. Cont Shelf Res 28:318–337

Lozovatsky ID, Liu Z, Hao W, Fernando HJS (2008b) Tides and mixing in the northwestern East China Sea. Part II: the near-bottom turbulence. Cont Shelf Res 28:338–350

Lozovatsky ID, Roget E, Planella J, Fernando HJS, Liu Z (2010) Intermittency of near-bottom turbulence in tidal flow on a shallow shelf. J Geophys Res 115, C05006. doi:10.1029/2009JC005325

Lozovatsky I, Liu Z, Fernando H, Armengol J, Roget E (2012) Shallow water tidal currents in close proximity to the seafloor and boundary-induced turbulence. Ocean Dyn 62:177–191. doi:10.1007/s10236-011-0495-3

Lueck RG, Lu Y (1997) The logarithmic layer in a tidal channel. Cont Shelf Res 17:1785–1801

MacKinnon JA, Gregg MC (2003) Mixing on the late-summer New England Shelf—solibores, shear, and stratification. J Phys Oceanogr 33:1476–1492

MacKinnon JA, Gregg MC (2005) Spring mixing: turbulence and internal waves during restratification on the New England shelf. J Phys Oceanogr 35:2425–2443

Moum JN, Nash JD (2000) Topographically induced drag and mixing at a small bank on the continental shelf. J Phys Oceanogr 30:2049–2054

Moum JN, Klymak JM, Nash JD, Perlin A, Smyth WD (2007) Energy transport by nonlinear internal waves. J Phys Oceanogr 37:1968–1988

Munk WH, Anderson ER (1948) Notes on the theory of the thermocline. J Mar Res 3:276–295

Nash J, Kunze E, Toole M, Schmitt R (2004) Internal tide reflection and turbulent mixing on the continental slope. J Phys Oceanogr 34:1117–1134

Orr MH, Mignerey PC (2003) Nonlinear internal waves in the South China Sea: observation of the conversion of depression internal waves to elevation internal waves. J Geophys Res 108, C33064. doi:10.1029/2001JC001163

Palmer MR, Rippeth TP, Simpson JH (2008) An investigation of internal mixing in a seasonally stratified shelf sea. J Geophys Res 113, C12005. doi:10.1029/2007JC004531

Perlin A, Moum JN, Klymak JM, Levine MD, Boyd T, Kosro PM (2005) A modified law-of-the-wall applied to oceanic bottom boundary layers. J Geophys Res 110:C10S10. doi:10.1029/2004JC002310

Phillips OM (1966) The dynamics of the upper ocean. Cambridge University Press, Cambridge, p 261

Polzin KL, Toole JM, Schmitt RW (1995) Finescale parameterizations of turbulent dissipation. J Phys Oceanogr 25:306–328

Prandke H, Stips A (1998) Test measurements with an operational microstructure-turbulence profiler: detection limits of dissipation rates. Aquat Sci 60:191–209

Ramp SR, Tang TY, Duda TF, Lynch JF, Liu AK, Chiu C-S, Bahr F, Kim H-R, Yang YJ (2004) Internal solitons in the northeastern South China Sea. Part I: source and deep water propagation. IEEE J Oceanic Eng 29:1157–1181

Ramp SR, Yang TYJ, Bahr FL (2010) Characterizing the nonlinear internal wave climate in the northeastern South China Sea. Nonlinear Proc Geophys 17:481–498

Rippeth TP, Palmer MR, Simpson JH, Neil R, Fisher NR, Sharples J (2005) Thermocline mixing in summer stratified

continental shelf seas. Geophys Res Lett 32, L05602. doi:10.1029/2004GL022104

Roget E, Lozovatsky ID, Sanchez X, Figueroa M (2006) Microstructure measurements in natural waters: methodology and applications. Prog Oceanogr 70:126–148

Sanford TS, Lien R-C (1999) Turbulent properties in a homogeneous tidal boundary layer. J Geophys Res 104:1245–1257

Schafstall J, Dengler M, Brandt P, Bange H (2010) Tidal-induced mixing and diapycnal nutrient fluxes in the Mauritanian upwelling region. J Geophys Res 115, C10014. doi:10.1029/2009JC005940

Scotti A, Beardsley R, Butman B (2006) On the interpretation of energy and energy fluxes of nonlinear internal waves: an example from Massachusetts Bay. J Fluid Mech 561:103–112

Sharples J, Moore CM, Abraham ER (2001) Internal tide dissipation, mixing, and vertical nitrate flux at the shelf edge of NE New Zealand. J Geophys Res 106:14069–14081

Shaw P-T, Ko DS, Chao S-Y (2009) Internal solitary waves induced by flow over a ridge: with applications to the northern South China Sea. J Geophys Res 114, C02019. doi:10.1029/ 2008JC005007

Simmons H, Chang M-H, Chang Y-T, Chao S-Y, Fringer O, Jackson CR, Ko DS (2011) Modeling and prediction of internal waves in the South China Sea. Oceanography 24:88–99

Simpson JH, Crawford WR, Rippeth TP, Campbell AR, Cheok JVS (1996) The vertical structure of turbulent dissipation in shelf seas. J Phys Oceanogr 26:1579–1590

Souza AJ, Howarth MJ (2005) Estimates of Reynolds stress in a highly energetic shelf sea. Ocean Dyn 55:490–498. doi:10.1007/s10236-005-0012-7

St. Laurent L (2008) Turbulent dissipation on the margins of the South China Sea. Geophys Res Lett 35, L23615. doi:10.1029/2008GL035520

St. Laurent L, Simmons H, Tang TY, Wang YH (2011) Turbulent properties of internal waves in the South China Sea. Oceanography 24:78–87

Stips A (2005) Dissipation measurements: theory. In: Baumert H, Simpson JH, Suendermann J (eds) Marine turbulence: theories, observations and methods. Cambridge University Press, Cambridge, pp. 115–126

Sundfjord A, Fer I, Kasajima Y, Svendsen H (2007) Observations of turbulent mixing and hydrography in the marginal ice zone of the Barents Sea. J Geophys Res 112, C05008. doi:10.1029/2006JC003524

Tian J, Yang Q, Zhao W (2009) Enhanced diapycnal mixing in the South China Sea. J Phys Oceanogr 39:3191–3203

Turner JS (1973) Buoyancy effects in fluids. Cambridge University Press, Cambridge, p 382

Umlauf L, Arneborg L (2009) Dynamics of rotating shallow gravity currents passing through a channel. Part I: observation of transverse structure. J Phys Oceanogr 39:2385–2401. doi:10.1175/2009JPO4159.1

van der Lee E, Umlauf L (2011) Internal wave mixing in the Baltic Sea: near-inertial waves in the absence of tides. J Geophys Res 116, C10016. doi:10.1029/2011JC007072

Wijesekera H, Padman L, Dillon T, Levine M, Paulson C (1993) The application of internal-wave dissipation models to a region of strong mixing. J Phys Oceanogr 23:269–286

Woods JD (1968) Wave-induced shear instability in the summer thermocline. J Fluid Mech 32:791–800

Yang Y-J, Tang TY, Chang MH, Liu AK, Hsu M-K, Ramp SR (2004) Solitons northeast of Tung-Sha Island during the ASIAEX Pilot Studies. IEEE J Oceanic Eng 29:1182–1199

Zhao Z, Klemas V, Zheng Q, Yan X-H (2004) Remote sensing evidence for baroclinic tide origin of internal solitary waves in the northeastern South China Sea. Geophys Res Lett 31, L06302. doi:10.1029/2003GL019077

Zheng Q, Susanto RD, Ho C-R, Song YT, Xu Q (2007) Statistical and dynamical analysis of generation mechanisms of solitary internal waves in the northern South China Sea. J Geophys Res 112, C03021. doi:10.1029/2006JC003551